

AMRVAC and Relativistic Hydrodynamic simulations for GRB afterglow phases

Zakaria Meliani^{1,2}*, Rony Keppens^{1,3,4}, Fabien Casse⁵ and Dimitrios Giannios²

¹ FOM-Institute for Plasma Physics Rijnhuizen P.O. Box 1207 3430 BE Nieuwegein, Netherlands

² Max Planck Institute for Astrophysics, Box 1317, D-85741 Garching Germany

³ Centre for Plasma Astrophysics, K.U.Leuven, Belgium

⁴ Sterrenkundig Instituut, Utrecht, Netherlands

⁵ AstroParticule & Cosmologie (APC)

UMR 7164 CNRS - Université Paris 7, 10 rue Alice Domon et Léonie Duquet 75025 Paris Cedex 13, France

Accepted; Received

ABSTRACT

We apply a novel adaptive mesh refinement code, AMRVAC, to numerically investigate the various evolutionary phases in the interaction of a relativistic shell with its surrounding cold Interstellar Medium (ISM). We do this for both 1D isotropic as well as full 2D jetlike fireball models. This is relevant for Gamma Ray Bursts, and we demonstrate that, thanks to the AMR strategy, we resolve the internal structure of the shocked shell-ISM matter, which will leave its imprint on the GRB afterglow. We determine the deceleration from an initial Lorentz factor $\gamma = 100$ up to the almost Newtonian $\gamma \sim O(2)$ phase of the flow. We present axisymmetric 2D shell evolutions, with the 2D extent characterized by their initial opening angle. In such jetlike GRB models, we discuss the differences with the 1D isotropic GRB equivalents. These are mainly due to thermally induced sideways expansions of both the shocked shell and shocked ISM regions. We found that the propagating 2D ultrarelativistic shell does not accrete all the surrounding medium located within its initial opening angle. Part of this ISM matter gets pushed away laterally and forms a wide bow-shock configuration with swirling flow patterns trailing the thin shell. The resulting shell deceleration is quite different from that found in isotropic GRB models. As long as the lateral shell expansion is merely due to ballistic spreading of the shell, isotropic and 2D models agree perfectly. As thermally induced expansions eventually lead to significantly higher lateral speeds, the 2D shell interacts with comparably more ISM matter and decelerates earlier than its isotropic counterpart.

Key words: Gamma Rays: Afterglow, Hydrodynamics, Theory – ISM: jets and outflows – Galaxies: jets, ISM – methods: numerical, relativity, AMR

1 INTRODUCTION

Many high energy astrophysical phenomena involve relativistic flows and shocks. For example, relativistic flows are invoked to explain the observed properties of various compact astrophysical objects (Arons 2004; Ferrari 1998; Corbel 2004). Astrophysical relativistic flows can reach a Lorentz factor of 2 – 10 in association with jets from Seyfert and radio loud galaxies (Piner et al. 2003), or even go up to Lorentz factors $10^2 – 10^3$ for Gamma Ray Burst (GRB) scenarios (Sari & Piran 1999; Soderberg & Ramirez-Ruiz 2001; Mészáros 2006). In the last decade, continued development of numerical algorithms and the increase in computer power have allowed to significantly progress in high-resolution, hydrodynamic numerical simulations in both special and general relativity (see

Marti & Müller 2003). The enormous time and length scale ranges associated with violent astrophysical phenomena in relativistic hydrodynamics (RHD), make Adaptive Mesh Refinement (AMR) an important algorithmic ingredient for computationally affordable simulations. RHD numerical simulations, particularly when combined with AMR capabilities, can investigate many details of relativistic flow regimes relevant for astrophysics.

In this paper, we concentrate on relativistic dynamics in the fireball model for the afterglow phases of GRBs, in one and two dimensional simulations. Since the follow-up detection of GRBs in X-ray (Costa et al. 1997) and their afterglows at longer wavelengths (Sahu et al. 1997; Van Paradijs et al. 1997; Galama et al. 1997; Frail et al. 1997; Piro et al. 1998), the cosmological origin of GRBs has been established (Metzger 1997; Wijers 1997). These detections confirmed the predictions from the fireball theoretical model (Rhoads 1993; Katz 1994; Mészáros & Rees 1997; Vietri

* E-mail: meliani@rijnh.nl

1997). In this model, a compact source releases a large amount of energy in a very short timescale, producing a fireball expanding with relativistic velocity. Its internal energy gets fully converted to kinetic energy, leading to a shell expanding with very high Lorentz factor. This cold shell continues to expand and interact with the circumburst medium, producing a relativistic shock-dominated evolution. As the shell sweeps up the matter, it begins to decelerate. Here, we investigate the details of such propagating relativistic shells with the relativistic hydrodynamics code AMRVAC (Bergmans et al. 2004). The AMRVAC code (Keppens et al. 2003) is here for the first time applied to the numerically challenging regime of high Lorentz factor, and we therefore include a variety of test problems, demonstrating the robustness as well as the limitations of our computational strategy.

Up till recently, analysis of GRB flows have largely been done analytically (Shemi & Piran 1990; Sari & Piran 1995; Mészáros & Rees 1997; Chiang & Dermer 1999), combined with numerical approaches usually employing a Lagrangian code. These latter works mainly investigate spherically symmetric GRB scenarios for obvious computational convenience (Panaiteescu et al. 1997; Kobayashi et al. 1999; Kobayashi & Sari 2000). Recently, some analytical works started to investigate the multidimensional jet structure in GRBs (Rhoads 1997, 1999; Panaiteescu & Mészáros 1999; Sari et al. 1999; Kumar & Panaiteescu 2000; Panaiteescu & Kumar 2003; Cheng et al. 2001; Oren et al. 2004; Kumar & Granot 2003), and some numerical simulations emerged as well, but restricted to relatively low (order 25) Lorentz factor (Granot et al 2001; Cannizzo et al. 2004). Higher speeds were obtained in the numerical simulation of the propagation of an axisymmetric jet through a collapsing rotating massive star, as investigated by Aloy et al. (2000) to analyse the first phase of GRBs. In these simulations, the jet is further followed after breakout to a maximum Lorentz factor of $\gamma_{\max} \sim 44$, which is still relatively small to the values required for GRBs by the fireball model. Therefore, an important area of current investigations in GRB context is to model the dynamics of narrow jets of ultra-relativistically flowing ejecta. This is motivated by the need to reduce the total amount of energy released in GRBs, by assuming these jets to point towards the observer, as compared to fully isotropic equivalents. This need is particularly clear for the exemplary cases of GRB 990123 (Kulkarni et al. 1999), GRB 050820A (Cenko et al. 2006), and GRB 050904 (Frail et al. 2006).

The detection of polarization (Covino et al. 1999; Wijers et al. 1999; Greiner et al. 2003; Lazzati et al. 2004) gave further support to the jetlike model. Evidence for narrow collimated outflows in GRBs is sustained also by the achromatic breaks in the afterglow light curves which was predicted analytically (Rhoads (1997, 1999); Sari et al. (1999)) and then observed in a large number of GRBs (Stanek et al. 1999; Sari et al. 1999; Berger et al. 2000; Panaiteescu 2005; 2006; Barthelmy et al. 2005). In Bloom et al. (2003), various GRBs were analysed and in 16 of them, the combination of these breaks in the spectrum and the jet-like model was used to deduce their effective energy, which was about $E \sim 10^{51}$ ergs. The half opening angle of such jets in GRBs is inferred to be of order few degrees. As a result, the afterglow producing shocked region is collimated too, with a similar initial opening angle (Frail et al 2001; Berger et al. 2003; Cenko et al. 2006; Panaiteescu 2005; Dar & De Rújula 2004). In our 2D simulations, we will concentrate on the afterglow phases in the GRB evolution starting from collimated ejecta, and discuss those dynamical effects causing opening angle changes in detail. Direct comparison with

the evolution of an equivalent 1D spherical shell is enlightening in this respect.

This paper is organised as follows. We start by reviewing the relativistic hydrodynamic equations. In Section 3, we include several tests to demonstrate the AMRVAC code potential for realistic RHD computations. In Section 4, we present our main astrophysical application to GRB flows in 1D and 2D models.

2 RELATIVISTIC HYDRODYNAMIC EQUATIONS

The special relativistic hydrodynamic evolution of a perfect fluid is governed by the conservation of the number of particles, and energy-momentum conservation. These two conservation laws can be written as

$$(\rho u^\mu)_\mu = 0, \quad (T^{\mu\nu})_\mu = 0. \quad (1)$$

where $\rho, \vec{u} = (\gamma, \gamma \vec{v})$, and $T^{\mu\nu} = \rho h u^\mu u^\nu + p g^{\mu\nu}$ define, respectively, the proper density, the four-velocity and the stress-energy tensor of the perfect fluid. Their definition involves the Lorentz factor γ , the fluid pressure p , and the relativistic specific enthalpy $h = 1 + e + p/\rho$ where e is the specific internal energy. For the (inverse) metric $g^{\mu\nu}$, we take the Minkowski metric. Units are taken where the light speed equals unity.

These equations can be written in conservative form involving the Cartesian coordinate axes and the time axis of a fixed ‘lab’ Lorentzian reference frame as

$$\frac{\partial U}{\partial t} + \sum_{j=1}^3 \frac{\partial F^j}{\partial x^j} = 0. \quad (2)$$

The conserved variables can be taken as

$$U = [D = \gamma \rho, \vec{S} = \gamma^2 \rho h \vec{v}, \tau = \gamma^2 \rho h - p - \gamma \rho]^T, \quad (3)$$

and the fluxes are then given by

$$F = [\rho \gamma \vec{v}, \gamma^2 \rho h \vec{v} \vec{v} + p \mathbf{I}, \gamma^2 \rho h \vec{v} - \gamma \rho \vec{v}]^T, \quad (4)$$

where \mathbf{I} is the 3×3 identity matrix. To close this system of equations, we use the equation of state (EOS) for an ideal gas, which is the polytropic equation with the polytropic index Γ ,

$$p = (\Gamma - 1) \rho e. \quad (5)$$

At each time step in the numerical integration, the primitive variables (ρ, \vec{v}, p) involved in flux expressions should be derived from the conservative variables U resulting in a system of nonlinear equations. One can bring this system into a single equation for the pressure p ,

$$\tau + D - \gamma(p) D - \frac{p + \Gamma p(\gamma(p)^2 - 1)}{\Gamma - 1} = 0, \quad (6)$$

which, once solved for p yields $\vec{v} = \frac{\vec{S}}{\tau + p + D}$. This nonlinear equation (6) is solved using a Newton-Raphson algorithm.

3 TESTING AMRVAC

In view of the challenges in the numerical investigation of relativistic fluids, we include here several substantial test results for code validation. We performed a large series of tests, some of them shown in this section. An important subclass of test cases is formed by Riemann problems, whose numerical solution can be compared to analytical solutions. Other, 2D tests shown here have no known

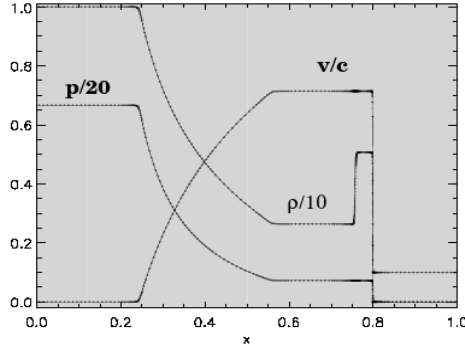


Figure 1. One-dimensional relativistic shock problem in planar geometry at $t = 0.36$. The solid lines are the analytical solution.

analytical solution. Therefore, we compare the results of our simulations with similar results previously obtained by other codes as documented in the astrophysical literature.

The Adaptive Mesh Refinement version of the Versatile Advection Code (AMRVAC) is specifically designed for simulating dynamics governed by a system of (near-)conservation laws. Available equations are the Euler and magnetohydrodynamic systems, in both classical and special relativistic versions. The discretization is finite volume based, and various shock-capturing algorithms can be used. The automated AMR strategies implemented vary from the original patch-based to a novel hybrid block-based approach (Van der Holst & Keppens 2006). These procedures generate or destruct hierarchically nested grids with subsequently finer mesh spacing. The refinement criterion used in AMRVAC is based on a Richardson type error estimator (Keppens et al. 2003). In all following tests, we use a refinement ratio of 2 between consecutive levels, unless stated otherwise.

3.1 One-dimensional test problems

3.1.1 Riemann problems

In 1D Riemann problems, we follow the evolution of an initial discontinuity between two constant thermodynamical states. In 1D RHD, we then typically find the appearance of up to three nonlinear waves. Generally, one finds a shock wave propagating into the lower density/pressure medium, a rarefaction wave propagating at sound speed into the denser medium, and between these two states, there can be a contact discontinuity. In the tests that follow, calculations are done in Cartesian geometry on a spatial domain $0 \leq x \leq 1$. The exact solutions for Riemann problems in relativistic hydrodynamics are discussed for vanishing tangential speed (i.e. y or/and z components for velocities) in Marti & Müller (1994) and for arbitrary tangential flow velocity in Pons et al. (2000).

In a first, mild test, we assume an ideal gas with polytropic index $5/3$ and initial constant states characterized by $p_L = 13.3$, $\rho_L = 10.0$ (left) and $p_R = 0.66 \times 10^{-6}$, $\rho_R = 1.0$ (right), separated at the location $x = 0.5$. The results at $t = 0.36$ are shown in Fig. 1 with a resolution of 100 cells on the base level and 4 levels, where we also overplot the exact solution. In the table 1, we present the $L_1 = \sum (\Delta x_j) |\rho_j - \rho(x_j)|$ norm errors of the density ρ , where $\rho(x_j)$ is the exact solution. The accuracy of our result is comparable to that of Lucas-Serrano et al. (2004); Zhang & MacFadyen (2006).

In a second test, we look particularly into effects due to

Table 1. L_1 errors of the density for the 1D Riemann problem 1 with uniform grid shown at $t = 0.36$

Number of grid points	L_1
200	1.15×10^{-1}
400	6.4×10^{-2}
800	3.2×10^{-2}
1600	1.9×10^{-2}
3200	1.06×10^{-2}

nonvanishing tangential velocities, for two ideal gases with polytropic index $\Gamma = 5/3$. We separate two different constant states $p_L = 10^3$, $\rho_L = 1.0$ (left) and $p_R = 10^{-2}$, $\rho_R = 1.0$ (right). For the transverse velocity we form nine combinations of the pair $v_{y,L}$ and $v_{y,R}$. As in Pons et al. (2000); Mignone et al. (2005), we take $v_{y,L} = (0.0, 0.9, 0.99)c$ in combination with $v_{y,R} = (0.0, 0.9, 0.99)c$. The spatial separation between the two states is initially at $x = 0.5$. The results at $t = 0.4$ are shown in Fig. 2, where we also overplot the exact solution using the code in Marti & Müller (2003).

The relativistic effects in these tests are mainly thermodynamical in the first mild test, and are due to coupling between the thermodynamics (through specific enthalpy) and kinetic properties (by the initial tangential velocities). For small tangential velocity cases, we use only a resolution of 200 cells on the base level and 4 levels. However, for a high tangential velocity case, we use high base resolution 400 with 10 levels to resolve the contact discontinuity and the tail of the rarefaction wave. In fact, for a high tangential velocity at left (in the high pressure state), the effective inertia of the left state increases. This makes the occurring shock move slower and decreases the distance between the tail of the rarefaction wave and the contact discontinuity. As also found in Zhang & MacFadyen (2006), it remains a numerical challenge to capture the contact discontinuity properly, which we only managed here by allowing a very high effective resolution.

3.1.2 Shock Heating Test

In another 1D test case, a cold fluid hits a wall and a shock front propagates back into the fluid, compressing and heating it as the kinetic energy is converted into internal energy. Behind the shock, the fluid becomes at rest. This test has an analytical solution in planar symmetry as considered by Blandford & McKee (1976), and the jump conditions are

$$\begin{aligned} p_2 &= \rho_1 (\gamma_1 - 1) (\gamma_1 \Gamma + 1), \\ \rho_2 &= \rho_1 \frac{\gamma_1 \Gamma + 1}{\Gamma - 1}, \\ v_{sh} &= (\Gamma - 1) \frac{\gamma_1 v_1}{\gamma_1 + 1}. \end{aligned} \quad (7)$$

These give the post shock pressure p_2 and density ρ_2 values in terms of the incoming density and Lorentz factor, together with the shock propagation velocity v_{sh} .

In our test we take the same initial conditions as in the recent paper by Zhang & MacFadyen (2006), where a cold fluid $p = 10^{-4}$ with a density $\rho = 1.0$ has an impact velocity of $v_1 = (1.0 - 10^{-10})$. This corresponds to a Lorentz factor $\gamma = 70710.675$. The temperature after the shock becomes relativistic, and therefore we take the polytropic index $\Gamma = 4/3$. Hence the shock velocity is $v_{sh} = 0.33332862$. The AMR simulation is done with 20 cells on the base level and 4 levels on the spatial range $0 < x < 1$. The result at $t = 2$, with the reflective wall at $x = 1$, is shown in Fig. 3.

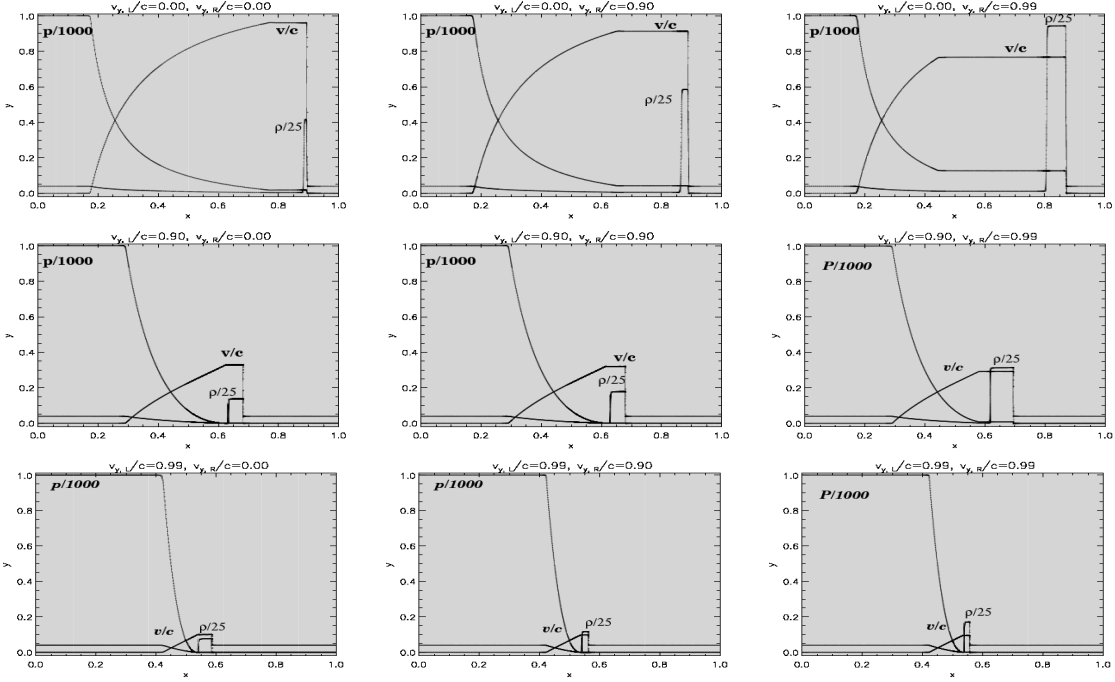


Figure 2. One-dimensional relativistic shock problems in planar geometry with tangential velocities v_y . The results presented correspond to $t = 0.4$. The solid lines are the analytical solution (Pons et al. 2000); from left to right $v_{y,R} = (0, 0.9, 0.99)c$, and from top to bottom $v_{y,L} = (0, 0.9, 0.99)c$.

The exact solution is overplotted as well. In this test, because of the constant state behind the shock, the maximum impact Lorentz factor that can be achieved numerically is limited only by the precision of the Newton-Raphson subroutine. This test is important to demonstrate its accurate treatment, in view of the intended simulations aimed at afterglows in GRBs. Indeed, in the shell-frame, the circumburst medium hits the dense shell with a high Lorentz factor. In a process similar to what is found in the above test, the kinetic energy of the impacting medium is converted to thermal energy of the external medium. Viewed in the lab frame, the swept up circumburst medium will have similarly high Lorentz factor and will form a hot shocked layer ahead of the contact interface. Note also that Fig. 3 indicates that our discretization and wall treatment does not suffer from the visible density errors seen in Zhang & MacFadyen (2006).

3.2 Two-dimensional tests

3.2.1 A relativistic 2D Riemann problem

A two dimensional square region is divided into four equal areas with a constant state each. We fix the polytropic index $\Gamma = 5/3$ and assume free outflow boundary conditions. The relativistic version of this test was proposed by Del Zanna & Bucciantini (2002) and subsequently reproduced by Lucas-Serrano et al. (2004); Zhang & MacFadyen (2006) and under slightly improved initial conditions by Mignone et al. (2005). We repeat this simulation with the same initial configuration from Del Zanna & Bucciantini (2002), namely

$$\begin{aligned} (\rho, v_x/c, v_y/c, p)^{\text{NE}} &= (0.1, 0.0, 0.0, 0.01), \\ (\rho, v_x/c, v_y/c, p)^{\text{NW}} &= (0.1, 0.99, 0.0, 1.0), \end{aligned}$$

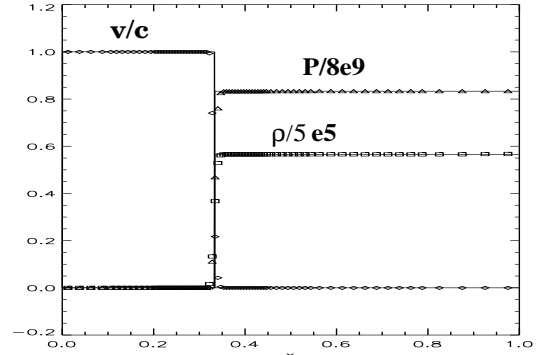


Figure 3. One-dimensional shock heating problem in planar geometry, where a cold fluid hits a wall located at $x = 1$. The results presented correspond to $t = 2$. The computational grid consists of 20 zones with 4 levels of refinement. The solid lines are the analytical solution.

$$\begin{aligned} (\rho, v_x/c, v_y/c, p)^{\text{SW}} &= (0.5, 0.0, 0.0, 1.0), \\ (\rho, v_x/c, v_y/c, p)^{\text{SE}} &= (0.1, 0.0, 0.99, 1.0). \end{aligned} \quad (8)$$

The simulation is done with 48×48 cells at the lowest grid level, and we allow for 4 levels. The result is shown in Fig. 4. Our result is in qualitative agreement with those results published, and shows the stationary contact discontinuities between SW-SE and SW-NW with a jump in the transverse velocity. These are somewhat diffused by the employed Total Variation Diminishing Lax-Friedrichs (TVDLF) discretization (Tóth & Odstrčil 2006). A simple and easily affordable remedy for improvement is to activate many more grid levels. Shocks feature across the interfaces NW-NE and SE-NE, propagating diagonally to the NE region, and an

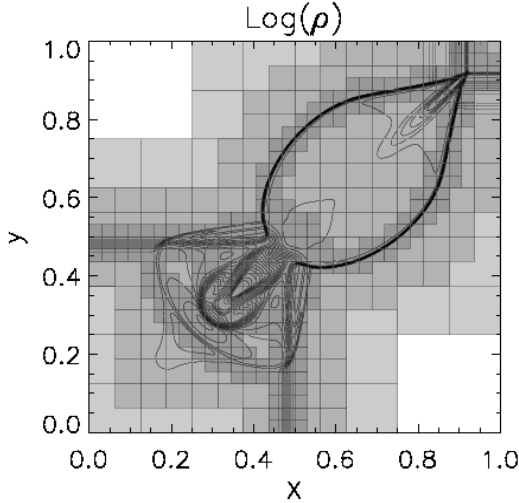


Figure 4. Density distribution for the two dimensional shock tube problem at $t = 0.4$. With a polytropic index $\Gamma = 5/3$, a base resolution of 48×48 and 4 AMR levels.

elongated diagonal shock structure forms as the NE sector recedes into the RHS top corner. In the SW corner, an oblique jet-like structure forms with a bow shock.

3.2.2 Relativistic jet in 2D cylindrical geometry

Since it is relevant for our 2D GRB simulations, we also present a two-dimensional simulation of an axisymmetric relativistic jet propagating in a uniform medium. We simulate the C2 jet model from Marti et al. (1997), but with an enlarged domain and at higher effective resolution. Our computational domain covers the region $0 < r < 15$ and $0 < z < 50$ jet radii. Initially, the relativistic jet beam occupies the region $r \leq 1, z \leq 1$, with $v_{\text{jet}} = 0.99$, $\rho_{\text{jet}} = 0.01$ and its classical Mach number $M = 6$. In this case, the jet is super-sonic but its temperature is still classical, so we can take the polytropic index $\Gamma = 5/3$. The density of the external medium is $\rho_{\text{ext}} = 1.0$. We follow the evolution until $t = 130$, and this end result is shown in Fig. 5. We performed the simulation with a resolution at the lowest level of the grid set to 90×300 , and allowed for a total of 5 levels of refinement eventually achieving an effective resolution of 1440×4800 .

In this simulation, the relativistic motion of the flow dominates, the thermal energy is weak compared to the kinetic energy. As a result the external medium influences only weakly the jet and the Lorentz factor $\gamma \sim 7$ flow produces a cocoon structure from the tip of the jet. One also finds a weak transverse expansion of the outflow in accord with what is reported by Marti et al. (1997). This transverse expansion of the jet is induced by the pressure build-up inside the cocoon Begelman & Cioffi (1989). In our simulation, the average transverse expansion obtained is occurring at an estimated speed of $v_T = 0.11 c$. Moreover, at the contact interface between shocked external medium and jet material, complex vortical structures form. These originate from Kelvin-Helmholtz type instabilities, as a consequence of cold fast jet outflow meeting a more static medium. The average propagation speed of the jet head is found to be $0.414 c$, which is in agreement with the one-dimensional analytical estimate of $0.42 c$ as given by Marti et al. (1997).

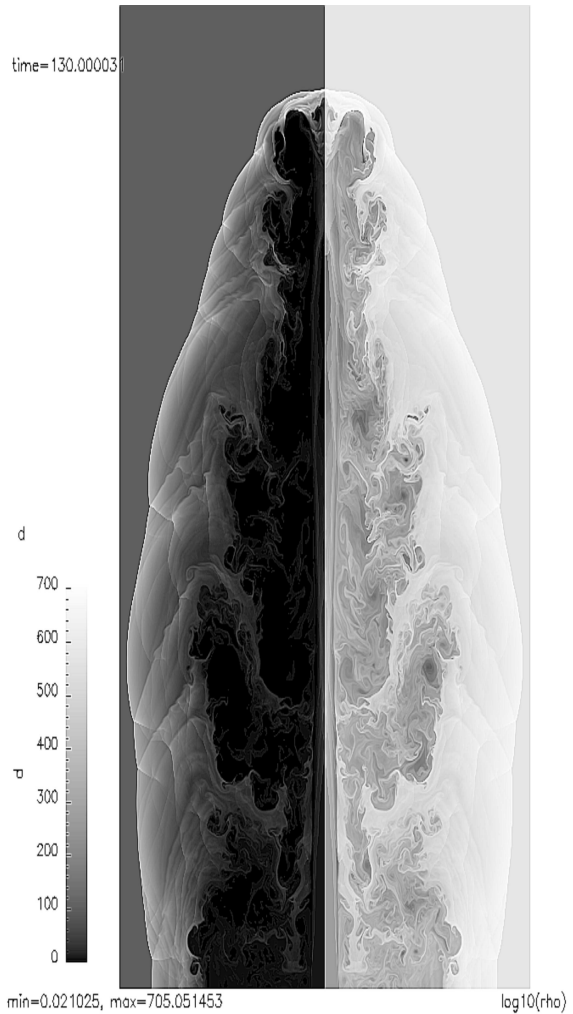


Figure 5. Density distribution for the axisymmetric relativistic jet at $t = 130$. At left, we show the lab frame density, at right, we show the proper density in a logarithmic scale. The computational base grid consists of 90×300 zones with 5 levels of refinement and the domain size is 15×50 .

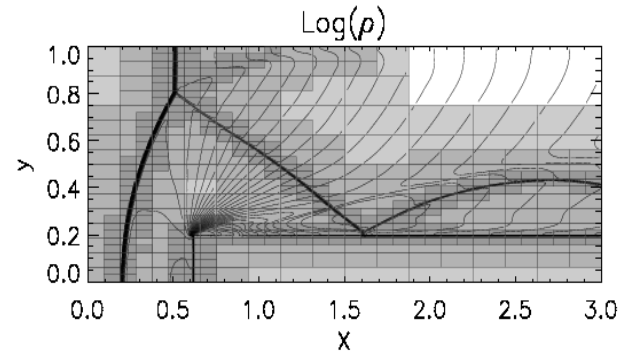


Figure 6. Density distribution, in logarithmic scale, for the forward facing step problem, at $t = 4.26$.

3.2.3 Wind tunnel with step

We reproduce here a standard test in the hydrodynamic literature, namely the forward facing step test from Emery (1968); Woodward & Colella (1984), but adjusted to the relativistic hydro regime as in Lucas-Serrano et al. (2004); Zhang & MacFadyen (2006). A horizontal relativistic supersonic flow enters a tunnel with a flat forward facing step. The test was done with a resolution 50×100 zones with 4 levels. The size of the tunnel is $0 \leq x \leq 3$ and $0 \leq y \leq 1$. The step is 0.2 in height and its position is at $x = 0.6$. It is treated as a reflecting boundary. The upper boundary and lower boundary for $x < 0.6$ are also both reflecting. However, the left boundary is fixed at the given inflow and the right one has free outflow. Initially, the whole computational domain is filled with ideal gas with $\Gamma = 7/5$ with a density $\rho = 1.4$ moving at $v_x = 0.999$, i.e., with a Lorentz factor $\gamma = 22.37$. The Newtonian Mach number is set to 3. The result of our simulation is shown in Fig. 6 at time $t = 4.26$. In this test, the relativistic flow collides with the step, as a result a reverse shock propagates back against the flow direction and this shock reflects from the upper boundary. A Mach stem forms and remains stationary. The result of our simulation is comparable to what is reported in Lucas-Serrano et al. (2004).

4 GRBS AND MODELS FOR THEIR AFTERGLOW PHASE

A popular model for GRB flows is known as the fireball model. In this model, GRBs are produced by a relativistic outflow following a violent event near a compact object. A large amount of energy is promptly released by the compact source in a region with small baryon loading (for a review see Piran (2005)). Initially, most of the energy of the flow is in the form of internal (thermal) energy. The shell expands rapidly converting its internal energy to kinetic. After the acceleration phase is complete, the shell is cold and moves with relativistic speeds.

This cold shell interacts with the circumburst medium, producing strong shocks. Our simulations will consider the dynamics from this phase onwards. As the shell sweeps up mass from the external medium, the kinetic energy in the relativistic shell is gradually transferred to kinetic and internal energy in the shocked ambient medium. Moreover, the shell itself gets traversed by a reverse shock, which in turn converts the kinetic energy of the shell to internal energy.

The observed afterglow emission that follows the prompt GRB emission is believed to come from synchrotron (with possible inverse Compton contribution) emitting electrons that are accelerated in the forward and reverse shocks (Sari et al. 1998; Galama et al. 1998). In the initial phases of the shell-ISM interaction, the electrons can be in the fast cooling regime (i.e. their cooling timescale is shorter than the expansion timescale) and, therefore, radiate efficiently most of the energy injected to them. Furthermore, if most of the energy dissipated in the shocks accelerates the electrons, then one has to consider radiative shocks. If either of the previous conditions does not hold, the radiative losses in the shocks are small. Here, we assume that the radiative losses are dynamically unimportant, i.e., the shocks are adiabatic throughout these simulations. According to the magnetization of the shell, the interaction shell-ISM and the spectrum could change as is shown in Mimica et al. (2006). Here, we assume that the magnetic field is dynamically unimportant.

4.1 1D isotropic shell evolution

In this simulation, we consider an ISM with uniform number density $n_{\text{ISM}} = 1 \text{ cm}^{-3}$. Many GRB afterglows (more than 25%) seem to be produced in such constant density medium (Chevalier & Li 2000; Panaitescu & Kumar 2002; Chevalier et al. 2004). This constant density medium can be the resultant of a Wolf-Rayet star progenitor, with its surroundings shaped by a weak stellar wind (Van Marle et al. 2006). Initially we set a uniform relativistic shell at $R_0 = 10^{16} \text{ cm}$ from the central engine, since according to Woods & Loeb (1995) the interaction of the shell with the ISM becomes appreciable at this distance. The shell has an initial Lorentz factor of $\gamma = 100$ (a $\gamma \geq 100$ is in accord with a shell which is optically thin to gamma-rays (Woods & Loeb 1995; Sari & Piran 1995)), and energy

$$E = 10^{54} \text{ ergs} = 4\pi\gamma^2 R_0^2 \delta \rho_{\text{shell}} c^2, \quad (9)$$

where δ stands for the lab-frame thickness of the shell set to $5 \times 10^{12} \text{ cm}$ is of the order of the expected value for a fireball $\delta \sim \max(c \Delta t, R_0/\gamma^2)$, where Δt is the duration of the GRB. The ISM and the shell are cold, and the initial pressure is set to $p_{\text{ISM}} = 10^{-3} n_{\text{ISM}} m_p c^2$ and $p_{\text{shell}} = 10^{-3} n_{\text{shell}} m_p c^2$ respectively. Note that this implies a huge initial contrast in the density measured in the lab-frame between the shell and the ISM $D_{\text{shell}}/D_{\text{ISM}} \sim 10^9$, and this presents an extreme challenge from a computational point of view. Initially, the energy of the shell is then mainly kinetic. We use a constant polytropic index $\Gamma = 4/3$, as the interaction shell-ISM will be dominated by the forward shock, where the temperature of the shocked ISM becomes relativistic.

In this simulation we use an effective resolution of 1536000 cells corresponding to the highest grid level 10 allowed. We use the full AMR capabilities in this simulation, since we simulate on a domain of size $[0.3, 300] \times 10^{16} \text{ cm}$, with 30000 grid points on the lowest level. At $t = 0$, the shell itself is then only resolved from grid level 6 onwards, when we use a refinement ratio of 2 between consecutive levels. The initial shell is resolved by about 25 cells in grid level 10 (later in the dynamical evolution this means that there are many more grid points throughout the widening structure). We use this very high effective resolution to avoid any numerical diffusion which may cause an artificial spreading of the shell. We ensure that throughout the entire simulation, grid level 10 is activated and concentrates fine grids on both the forward shock and reverse shock regions. Both are very important to determine the precise timing of the deceleration.

In Fig. 7, we show snapshots taken at lab-frame time $t \simeq 2.2 \times 10^6 \text{ s}$ corresponding to an early time in the entire simulation, and in Fig. 9, we show snapshots taken at time $t \simeq 1.5 \times 10^7 \text{ s}$ corresponding to a time when the shock is fully developed, we will concentrate our discussion mainly on this figure 9. These figures demonstrate that we resolve all four regions that characterise the interaction between an outward moving relativistic shell and the cold ISM. From right to left, we recognize (Fig. 9) (1) the ISM at rest, (2) the shocked ISM that has passed through the forward shock, with its Lorentz factor raised to $\gamma_{(2)} \sim 30$. This swept-up ISM gets compressed at the front shock and its number density reaches $n_{(2)} \sim 75 \text{ cm}^{-3} \sim \frac{\Gamma \gamma_{(2)} + 1}{\Gamma - 1}$ (Sari & Piran 1995). These two values correspond to the analytical estimate given by eq. (7) for the front shock propagation. Region (3) represents part of the initial shell material which is shocked by the reverse shock. The reverse shock propagates back into the cold shell, reducing its Lorentz factor and converting its kinetic to thermal energy. Transfer of energy from the initial cold shell thus occurs both at the forward and the re-

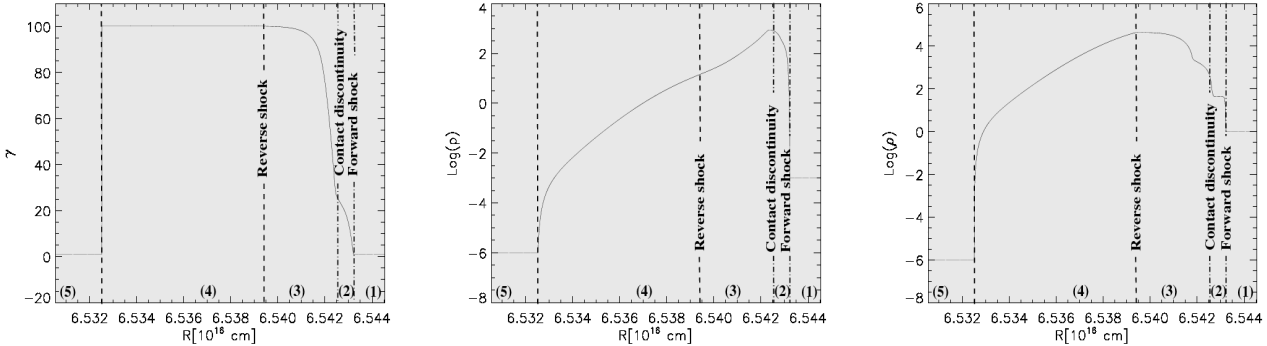


Figure 7. The five regions characterizing the interaction of the relativistic shell with the ISM at $t = 2.2 \times 10^6$ s. Panel(a): Lorentz factor, (b): logarithm of the pressure, (c): logarithm of density.

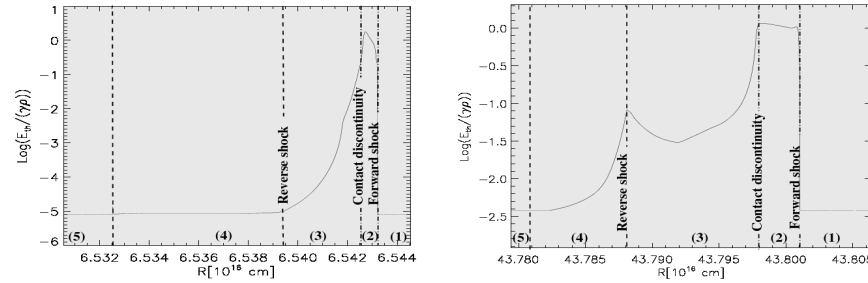


Figure 8. Ratio of thermal energy to mass energy, when the shell reaches distance: $R \approx 6.5 \times 10^{16}$ cm ($t \approx 2.2 \times 10^6$ s) (left), and $R \approx 4.3 \times 10^{17}$ cm ($t \approx 1.5 \times 10^7$ s) (right).

verse shock. Regions (2) and (3) are separated by a contact discontinuity (Mészáros & Rees 1992). At this spherical contact surface, the longitudinal velocity (Lorentz factor in 1D case) and pressure remain constant, but there is a jump in density. Furthermore, region (4) is the unshocked cold material of the shell, moving with a Lorentz factor $\gamma_{(4)} = 100$. The weak thermal energy of the shell interior itself did induce a slight expansion in the thickness of this part of the shell.

The reverse shock separating region (3) and (4) propagates into the cold shell with a Lorentz factor $\gamma_{RS} = \gamma_{(3)}\gamma_{(4)}(1 - v_{(3)}v_{(4)}/c^2) \sim 2.5$. This reverse shock is Newtonian inefficient in raising the thermal energy content as is shown in Fig. 8 (left panel), where we draw the specific thermal energy in the shocked ISM and shell when the shell reaches a distance $R \approx 6.5 \times 10^{16}$ cm. The reverse shock remains Newtonian until it reaches a distance from the GRB source of $R \sim 3.8 \times 10^{17}$ cm. Then it becomes mildly relativistic until $R \sim 4.3 \times 10^{17}$ cm where the reverse shock becomes very efficient to convert the kinetic energy to thermal energy (see Fig. 8 at right). Beyond this latter distance, the density of the unshocked shell part $\rho_{(4)}$ has decreased in accord with the spherical expansion of the shell, to $\rho_{(4)} \ll \gamma_{(4)}^2 \rho_{ISM}$. As a result, the reverse shock becomes relativistic. This behavior is characteristic for an initial thin cold relativistic shell decelerating in a constant density external medium. In fact, until the outward propagating shell reaches $R \sim 3.8 \times 10^{17}$ cm, the shocked ISM matter is hot $e_{(2)} \sim 30.0\rho_{(2)}$ (where $\gamma_{(2)} = 30$ corresponds to the analytical solution for the relativistic forward shock $e_{(2)} = (\gamma_{(2)} - 1)\rho_{(2)}$), while the shocked shell material which has $e_{(3)} = e_{(2)}$ is cold, since $e_{(3)} \sim 0.01\rho_{(3)}$. When the density in the non-shocked shell (i.e. $\rho_{(4)}$)

decreases enough due to spherical expansion, the Lorentz factor of the reverse shock increases and the last part of the shocked shell becomes hot $e_{(3)} \sim \rho_{(3)}$.

There is another region (5) indicated in the figures behind the shell. The density and the pressure in the region (5) are very small with $n_{(5),min} < 10^{-6}\text{cm}^{-3}$ and $p_{(5),min} < 10^{-6}m_p c^2$. Therefore, the region (5) is in the numerical point of view a vacuum. This region (5) is not of strong interest for the physics of the afterglow, but it is computationally challenging to resolve the interface between the regions (4) and (5) where the ratio of the lab frame density between the two reaches $D_{(4)}/D_{(5)} \sim 10^{14}$ in the first phase of the propagation of the shell ($R \sim 10^{16}$ cm), while the expansion of the shell remains weak. By the time shown in Fig. 7, this contrast has dropped to a value of at most 10^{12} .

The near-total deceleration of the shell only takes place when the two shocks in the shell-ISM interaction manage to convert an important fraction of the kinetic energy of the shell to thermal energy (and the efficiency of this conversion depends on whether the reverse shock is relativistic or Newtonian, as discussed above), while the rest is transferred to the swept-up ISM in the form of kinetic and thermal energy. In the first phase of the deceleration, the maximum Lorentz factor of the shell decreases gently from 100 at a distance of $R \sim 2.5 \times 10^{17}$ cm to 80 at a distance of $R \sim 4.3 \times 10^{17}$ cm. However, only at the latter distance of 4.3×10^{17} cm, a sudden decrease of the maximum Lorentz factor of the entire configuration from $\gamma = 80$ to $\gamma = 30$ takes place. This fast drop of the maximum Lorentz factor as seen in Fig. 10 coincides with the moment at which the reverse shock reaches the back end of the cold shell, thereby converting its kinetic to thermal energy (Fig. 9). In fact,

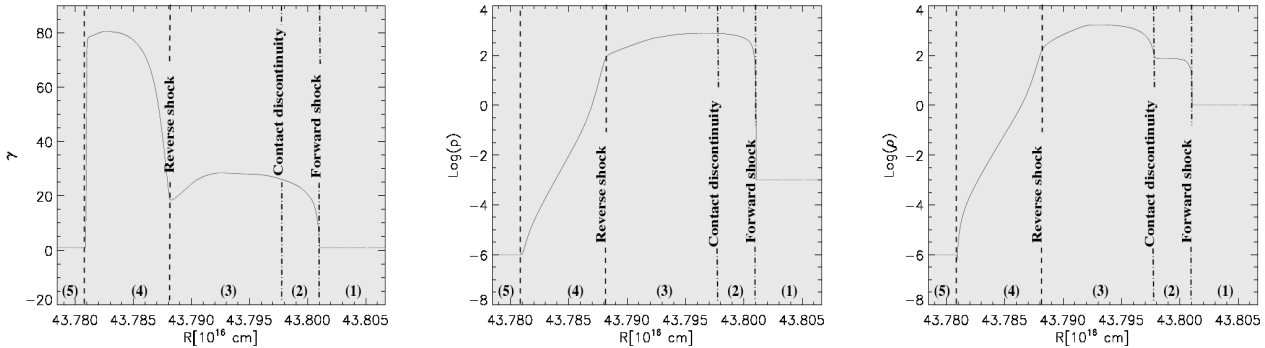


Figure 9. The five zones present when the relativistic shell interacts with the ISM at $t \approx 1.5 \times 10^7$ s. (a) Lorentz factor, (b) log of pressure, (c) log of density.

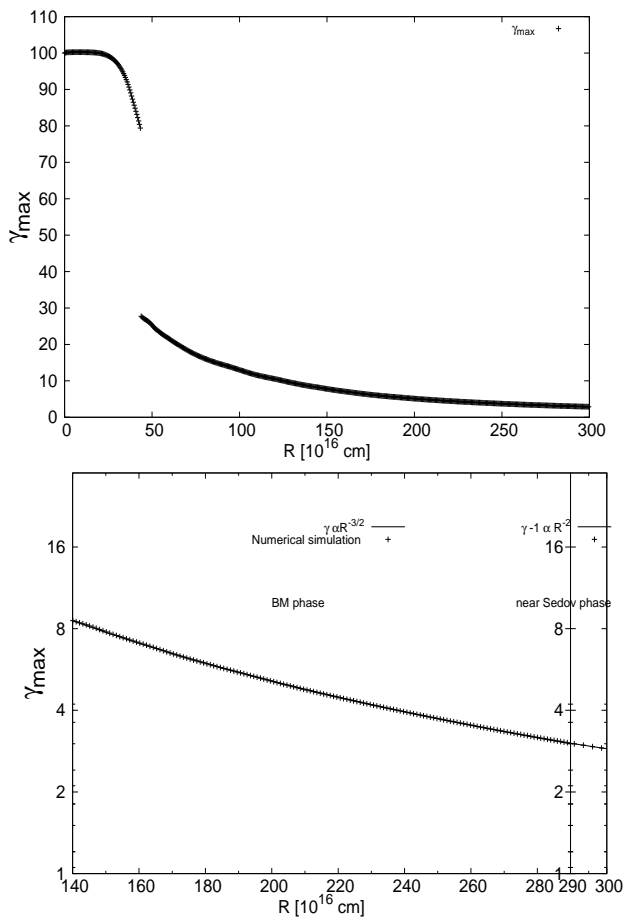


Figure 10. The variation of the maximal Lorentz factor in the propagating shell-ISM structure with time a) when the shell propagates from $R_0 = 10^{16}$ cm to $R = 300 \times R_0$ b) when the shell decelerates following the Blandford-McKee profile.

when plotting the maximal Lorentz factor as a function of distance, initially we always observe the Lorentz factor of the unshocked shell matter. As soon as the reverse shock has crossed the entire initial shell, we start to follow the evolution of the Lorentz factor of the shocked ISM (at the forward shock) where the maximum Lorentz factor is 30 at that particular moment.

After this phase, the shell structure continues to decelerate by transferring its kinetic energy to shocked ISM matter at the forward shock. However, as seen in Fig. 10, it still takes a certain time before the variation of maximum Lorentz factor now characterizing the shocked ISM matter follows the self-similar analytical solution for blast-wave deceleration as put forward by Blandford & McKee (1976). From about a distance of 1.2×10^{18} cm, our numerical solution starts to follow the analytical solution precisely. In fact, after the reverse shock traversed the entire initial shell, a forward traveling rarefaction wave propagates through the entire structure thereby slowing it down while transferring most of the energy to shocked ISM regions. This structure does not follow the self-similar prescription and causes the initial difference. In the end, the distance between the forward shock and the contact discontinuity increased sufficiently and the resulting radial thermodynamic profiles in between become fully described by the Blandford-McKee analytical solution. The Lorentz factor predicted by the Blandford-McKee solution behind the forward shock (for an adiabatic shock) is $\gamma_{BM} = (E/\rho_{ISM}^2 R^3)^{1/2} \propto R^{-3/2}$. The prediction of the Blandford-McKee solution for the Lorentz factor of the flow is also plotted in Fig. 10 and the agreement with the results of the simulation at these later stages of the deceleration is good.

Eventually, we enter into the mildly relativistic regime for the blast wave evolution. The transition to the Sedov-Taylor phase occurs beyond the simulated distance $R > 300 \times 10^{16}$ cm, since we still have a Lorentz factor of about 3 at the end of the simulation. The Sedov-Taylor distance we find is close to the analytical estimate given by $\ell \sim (3E/4\pi\rho_{ISM} c^2)^{1/3} \sim 5 \times 10^{18}$ cm.

4.2 2D modeling of directed ejecta

Precise analysis of the afterglow phases requires to evolve numerically confined ejecta in more than 1D, propagating in a jet-like fashion into the ISM. We now present axisymmetric, 2D simulations of a relativistic cold shell propagating in uniform ISM with a number density $n_{ISM} = 1 \text{ cm}^{-3}$. In this work, we investigate the uniform model jet (Rhoads 1999). The shell density and energy is set constant throughout the shell, and we take it to correspond to an isotropic spherical shell containing an equivalent isotropic energy $E_{iso} = 10^{51}$ ergs and a Lorentz factor $\gamma = 100$. To make the 2D computation feasible, we now start the simulation with a shell thickness $\delta = 10^{14}$ cm at a distance $R_0 = 10^{16}$ cm from the central engine. In the initial setup the shell occupies an annular region, with half opening angle of the shell equal to $\theta = 1^\circ$. This angle is

rather small with respect to those typically deduced from modeling of the optical light-curve breaks but still in agreement with the most collimated GRB flows (Bloom et al. 2003; Panaiteescu 2005). With the choice of a rather narrow jet, we expect the 2D effects to appear earlier and to be more pronounced with respect to a spherical shell with the same isotropic equivalent energy. Note that as a result, this jet like outflow has a decreased effective energy in the shell $E_{\text{jet}} = (\theta^2/2)E_{\text{iso}}$.

The AMR run uses 4 grid levels, taking 400×6000 at level 1, but with refinement ratios of 2, 4 and 2 between consecutive levels eventually achieving an effective resolution of 6400×96000 . The domain is $[0, 4] \times [0.3, 30]$ in R_0 units, as we specifically intend to model in detail the most dramatic phase of deceleration prior to the Blanford-McKee evolution. Note that we initially have $\gamma > 1/\theta$, which appears to be the case for a GRB jet. Beaming effects are invoked to explain the observed steepening in the decay light curve resultant from the transition $\gamma > 1/\theta$ (indistinguishable from an isotropic explosion) to $\gamma < 1/\theta$ (Panaiteescu & Mészáros 1999; Panaiteescu & Kumar 2002; Panaiteescu 2005). With these setup we can verify from our high resolution simulation whether up to times corresponding to the transition $\gamma \sim 1/\theta$, only the isotropic energy E_{iso} is relevant for the dynamics and the resulting emission (Piran 2000; Granot 2005).

The initial velocity of the shell is purely radial. Note that, compared to the 1D isotropic case presented in the previous section, the 2D simulation starts with an initial condition containing less energy. This is done for mere practical reasons: we wish to keep the computation feasible within two week's execution time on a single processor. Due to this lower energy content, the deceleration distance will be smaller by about one order of magnitude since less swept-up ISM mass is sufficient to decelerate the shell. This reduces the need for resolving many decades of propagation distance as measured in units of the initial shell thickness. In fact the 1D equivalent isotropic case with the same energy shows a sudden decrease of the maximum Lorentz factor of the decelerating configuration that corresponds to the reverse shock crossing of the shell at $R \sim 9 \times 10^{17}$ cm. This happens well before the simulated 3×10^{17} cm.

Fig. 11 shows at the (top), the sound speed contour, and the density distribution in a logarithmic scale in the (left), and the Lorentz factor in the (right). At the bottom, a zoom in the region around the shell is shown in the (left), the sound speed and the lateral velocity, in the (right) the Lorentz factor, and in the (center) a zoom only on the shell, the density and Lorentz factor. As in the 1D case, at first the shell propagates with a constant maximum Lorentz factor, and this is accompanied by a weak spread of the shell. Part of this radial shell widening in the bottom part of the shell is affected by the creation of a very low pressure and density region below the shell (also occurring in the 1D scenario). This near-vacuum state remains at the rear part as the shell moves away at the specified Lorentz factor. In this 2D simulation, the unshocked shell also spreads laterally with an initial transverse (horizontal) velocity, since the shell is launched with a pure radial velocity. The corresponding maximum initial lateral velocity of the unshocked shell is $v_T = 0.0175 c$. However, the shocked, swept up ISM matter spreads laterally much faster, due to its high thermal energy content. Initially, that shocked ISM part spreads with a comoving velocity of $v_{T,\text{co}} \sim 0.4c$, which is less than the maximum sound speed allowed by the polytropic equation of state $c/\sqrt{3}$. Due to this fast sideways expansion of shocked shell and ISM, the mass of the ISM hit by the shell grows faster than r^2 . Therefore, the deceleration of the shell starts earlier than in the isotropic case, see Fig 12. This result implies that the transition from the phase where E_{iso} is relevant,

to the phase where E_{jet} is relevant in the dynamics takes place when the shocked ISM and shell start to spread laterally much faster than what corresponds to pure radial (ballistic) flow.

In the last part of the shell-ISM deceleration phase, when the reverse shock has crossed the entire initial shell material, the lateral velocity of shocked shell material reaches a comoving speed of $v_{T,\text{co}} \sim 0.7c$. This means that we do find that the lateral velocity can be bigger than the sound speed in the medium which is in accord with the analytical result of Sari et al. (1999). This is at odds with numerical findings as those found in Cannizzo et al. (2004), which employ a much reduced resolution as compared to our AMR results (at low resolution, we do obtain a reduced lateral spreading velocity). As a result of this fast lateral spread of the shocked material, distinct differences occur in the deceleration stages as compared to the isotropic case. This result is very important, as it shows that the lateral spreading of the shell is not related only to the Lorentz factor of the shell but to the type of the reverse shock. In our computation, in an early phase the reverse shock is Newtonian and the expansion of the shocked shell part is modest. However, in a later phase the reverse shock becomes relativistic and this leads to faster lateral spreads. However, as the forward shock is always relativistic, already in an early stage the shocked ISM spreads with high velocity. The overall spreading of the shocked ISM and shocked shell configuration can, thus, be quite complex and rather more evolved than the one that semi-analytical models (Rhoads 1999; Panaiteescu & Mészáros 1999; Sari et al. 1999; Piran 2000) predict.

Only that part of the ISM found within the solid angle of the expanding shell is swept up, and this opening angle changes due to the spreading effects just discussed. In our 2D simulation, we found in analogy with the 1D (higher energy) case from above, that the reverse shock is initially Newtonian, so the thermal energy in the shocked part of the shell does not increase a lot and its lateral expansion remains weak for a while. Later on, its lateral expansion speed goes up to the $0.7c$ mentioned above, as the reverse shock becomes relativistic and the material through which the shocked shell expands laterally has already been brought to lower densities by the shocked ISM interaction.

The variation of the maximum Lorentz factor is less sudden than in the equivalent 1D spherical explosion, as quantified in Fig. 12. The part of the shell most distant from the symmetry axis decelerates before the more internal part. The shell sweeps up more matter than in the corresponding isotropic case in the external parts due to the lateral spreading effects discussed. In fact, in this simulation we may draw the analogy between the shell interaction with the ISM and simulations of relativistic AGN jet propagation into an external medium. As in those cases, the energy is transferred to the ISM through a bow shock structure. However, our modeled ejected shell representative of a burst in GRBs is not continually supported by injection of energy at the bottom. As a result, in the (small opening angle) shell there is not really evidence of a clear jet beam as in an AGN jet. In this case the interaction shell-ISM is dominated primarily by forward, reverse shock pair, and contact discontinuity in between. The changing 2D structure of this shock leads to differences in the shocked ISM mass loaded on to the shell. As stated earlier, only a fraction of the ISM within the opening angle of the shell is swept up, and an important part of ISM matter gets pushed away laterally as the thin radially confined shell advances. The resulting behavior is clearly influenced by these 2D effects, and is the reason why the maximum Lorentz factor of the configuration starts to decrease earlier than in the 1D scenario. In an isotropic scenario all swept up mass of the ISM remains in front

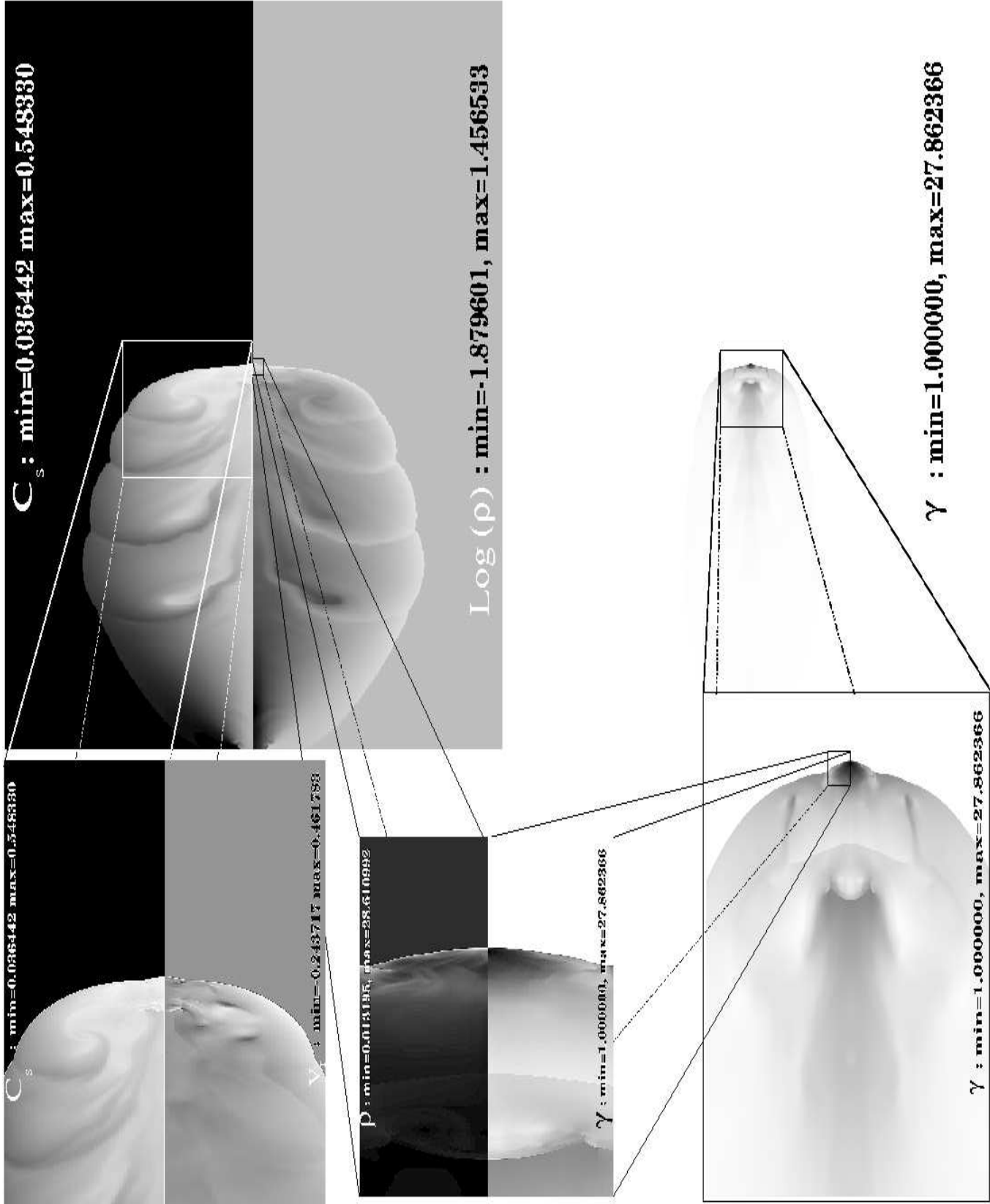


Figure 11. On the (top), the sound speed, logarithm of density (right), and Lorentz factor contours for the 2D simulation (left). On the (bottom), a zoom around on the relativistic shell, the sound speed and the lateral velocity (left), the Lorentz factor (right), and the zoom on the shell, the density and Lorentz factor (center) at $t = 5 \times 10^6$ s.

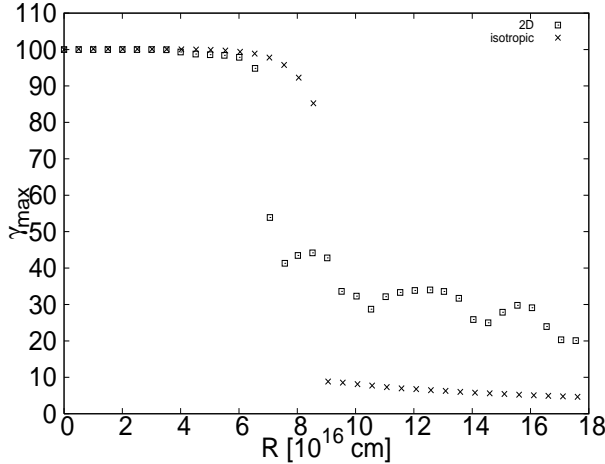


Figure 12. The variation of the maximum Lorentz factor evolution in 1D and 2D scenarios compared.

of the initial shell where most of the energy of the shell is continually transferred to shocked ISM. However, in the jet-like explosion, the shocked ISM and shell expand laterally leading to interaction with more ISM material, but the main part of this ISM material gets deflected about the shell. As seen in Fig 11, we find rather complex flow patterns trailing the thin shell. Hence, the mass accreted on to the shell in fact decreases as compared to the equivalent local isotropic scenario. Therefore, less energy is transferred continually to the shocked ISM.

One interesting characteristic of the maximum Lorentz factor of the beamed shell at radii $R > 7 \times 10^{16} \text{ cm}$ is the ‘‘bumps’’ that it shows as function of radius. These modulations of γ_{\max} are a result of rapid internal motions of the decelerating configuration caused by the complex shell-ISM interaction. In view to the very rich and unexpected early afterglow phenomenology revealed by the *SWIFT* satellite (see, for example, Zhang et al. (2006)), it is interesting to study whether these proper motions can cause a significant modulation in the emitted radiation expected from these flows.

In this simulation, we find no real indication of a strong change in lateral spreading of the shell when the Lorentz factor drops down to $\gamma_c = 1/\theta \sim 57$ (Rhoads 1999; Panaiteescu & Mészáros 1999). In fact, an important change is produced later, when the Lorentz factor of the shell becomes smaller than 30, while the lateral velocity of the shell reaches $v_{T,\text{co}} \sim 0.7c$. As pointed out, this coincides with the time when the reverse shock became relativistic and almost crossed the initial shell entirely. After this phase of rapid lateral spread, we find that the spread out shell decelerates faster, as it accumulates more matter (Fig. 11). More simulations with different values for the shell opening angle and thickness are to investigate how these parameters affect the phase of the deceleration where the lateral spreading of the shell becomes important.

5 CONCLUSIONS

In this paper, we presented and applied the AMRVAC code in its extension to relativistic hydrodynamics. The adaptive mesh refinement is particularly useful for simulating highly relativistic flow dynamics. We always used the robust TVDLF scheme, and this shock-capturing method together with high effective resolution delivers numerical results that can rival or even improve other high order

methods. As is well-known, difficulties in special relativistic hydrodynamic simulations result from the non linear coupling between different components of the velocity by the Lorentz factor and also the coupling between inertial and thermodynamics. We demonstrated that Adaptive Mesh Refinement (AMR) is then very useful to resolve the associated very thin structures properly. We tested the code ability with stringent recent test problems collected from the astrophysical literature, including 1D and 2D shock tube problems, an ultrarelativistic flow reflecting of a wall, a relativistic variant of a forward-faced reflecting step, and 2D astrophysical jet propagation.

We used the fireball model to investigate 1D and 2D afterglow phases in GRBs. In 1D, we examined the evolution of a cold relativistic shell with a Lorentz factor of 100 in uniform medium. In this simulation we discussed details of the internal structure of the evolving shell-ISM ejecta and compare them with analytical estimates. We followed the evolution of this isotropic explosion almost all the way into the classical Sedov phase. At all times, we resolve the various regions that characterize this interaction. We quantified and discussed the precise deceleration of the relativistic shell. When most of the initial energy of the shell is transferred to swept-up shocked ISM (this occurs at the forward shock), the deceleration of shocked ISM is eventually well described by the relativistic Blandford-McKee self-similar solution. Hence the Lorentz factor of the forward shock decreases as $R^{-3/2}$.

We investigate also the afterglow phase for a beamed 2D shell. In this model, we discussed analogies and important differences with the 1D model. The interaction of a confined relativistic shell with the ISM is characterised by the appearance of a bow shock. We showed how ISM material is laterally pushed out, thus decreasing the amount of accumulated matter in front of the shell near the axis. The part of the shell furthest away from the axis decelerates then faster than in a 1D spherical case. Although the deceleration of the shell starts early as compared to an equivalent isotropic case, the deceleration of the inner part of the shell is slow due to the weak accreted ISM matter in front of the shell. The thermal energy of the shocked ISM increases and induces a lateral spread of this shocked ISM. We have shown with a high resolution simulation of jet-like GRB models in their afterglow phase that this lateral expansion goes through various phases.

First, the shell spreads only with its initial lateral velocity until it accretes enough ISM matter. In this phase, the shocked ISM spreads laterally with a velocity near the sound speed. However, the reverse shock propagates in a Newtonian fashion through the shell, thus having a small efficiency in the conversion of the kinetic energy of the shell to thermal energy, hence the expansion of the shocked shell is still weak. Only in a later phase when the reverse shock becomes relativistic, the lateral expansion of the shocked shell increases drastically and reaches a high velocity $v_T \sim 0.7c$. The transition from slow to fast lateral spreading of the shell is thus related to the transition from Newtonian to relativistic reverse shock propagation. However, as the forward shock is always relativistic the shocked ISM spreads laterally faster.

The 2D simulation has revealed rapid internal motions in the decelerating configuration. It is possible that these motions result in modulations in the afterglow emission. In future work, we intend to use these and similar simulation results to compute their predictions for the precise afterglow spectral evolution.

ACKNOWLEDGEMENTS

We acknowledge financial support from the Netherlands Organization for Scientific Research, NWO-E grant 614.000.421, and computing resources supported by NCF. Part of the computations made use of the VIC cluster at K.U.Leuven. Part of this research was supported by European FP5 RTN "Gamma Ray Burst: An Enigma and a Tool".

REFERENCES

Aloy, M. A., Müller, E., Ibáñez, J. M., Martí, J. M., MacFadyen, A., 2000, *ApJ*, 531, L119

Arons, J., 2004, *Advances in Space Research*, 33, 466

Barthelmy S. D., et al., 2005, *ApJ*, 635, L133

Begelman, M. C., Cioffi, D. F., 1989, *ApJ*, 345, L21

Berger E., et al. 2000, *ApJ*, 545, 56

Berger, E., Kulkarni, S. R., Frail, D. A., 2003, *ApJ*, 590, 379

J. Bergmans, R. Keppens, D.E.A. van Odyck and A. Achterberg, Lecture Notes in Computer Science and Engineering, Proceedings of Chicago Workshop on Adaptive Mesh Refinement Methods Sept. 3-5 2003

Blandford, R. D., & McKee, D. G., 1976, *Physics of Fluids*, 19, 1130

Bloom, J. S., Frail, D. A., Kulkarni, S. R., 2003, *ApJ*, 594, 674

Cheng, K. S., Huang, Y. F., Lu, T., 2001, *MNRAS*, 325, 599

Cannizzo, J. K., Gehrels N., Vishniac E. T., 2004, *ApJ*, 601, 380

Cenko, S. B. et al., 2006, *astro-ph/0608183*

Chevalier, R. A., Li Z.-Y., 2000, *ApJ*, 536, 195

Chevalier, R. A., Li Z.-Y., Fransson, C., 2004, *ApJ*, 606, 369

Chiang J., Dermer C. D., 1999, *ApJ*, 512, 699

Corbel, X-ray Timing 2003: Rossi and Beyond. AIP Conference Proceedings, Vol. 714, held 3-5 November, 2003 in Cambridge, MA. Edited by Philip Kaaret, Frederick K. Lamb, and Jean H. Swank. Melville, NY: American Institute of Physics, 2004, 127

Costa, E., et al., 1997, *Nature*, 387, 783

Covino, S. et al., 1999, *A&A*, 348, L1

Dar, A., De Rujula, A. 2004, *Physics Reports*, 405, 203

Del Zanna, L., Bucciantini, N., 2002, *A&A*, 390, 1177

Donaghy, T. Q., 2006, *ApJ*, 645, 436

Emery, A. E., 1968, *J. Comput. Phys.*, 2, 306

Ferrari, A., 1998, *Annu. Rev. Astron. Astrophys.*, 36, 539

Frail, D. A., Kulkarni, S. R., Nicastro, S. R., Feroci, M., Taylor, G. B., 1997, *Nature*, 389, 261

Frail, D. A., et al., 2001, *ApJ*, 562, L55

Frail, D. A. et al., 2006, *ApJ*, 646, L99

Galama, T., et al., 1997, *Letters to Nature*, 387, 479

Galama, T. J., et al., 1998, *ApJL*, 500, L97

Gorosabel, J., et al., 2006 *astr-ph/0603100*

Granot, J., Miller, M., Piran, T., Suen, W. M., Hughes, P. A., 2001, Gamma-Ray Bursts in the Afterglow Era: Proceedings of the International Workshop Held in Rome, Italy, 17-20 October 2000, ESO ASTROPHYSICS SYMPOSIA. ISBN 3-540-42771-6. Edited by E. Costa, F. Frontera, and J. Hjorth. Springer-Verlag, 2001, 312

Granot, J., 2005, Triggering relativistic jets, *RevMexAA,astro-ph/0610379*

Greiner, J. et al. 2003, *Nature*, 426, 157

Katz, J. I., 1994, *ApJ*, 432, 107L

Keppens, R., Nool, M., Tóth, G., Goedbloed, J. P., 2003, 153, 317

Kobayashi S., Piran, T., Sari, R., 1999, *ApJ*, 513, 669

Kobayashi S., Sari, R., 2000, *ApJ*, 542, 819

Kulkarni, S. R. et al., 1999, *ApJ*, 522, 97L

Kumar, P., Panaiteescu, A. 2000, *ApJ*, 541, L9

Kumar, P., Granot, 2003, *ApJ*, 591, 1075

Lazzati, D., et al. , 2004, *A&A*, 422, 121L

Lucas-Serrano, A., Font, J. A., Ibáñez J. M., and Martí, J. M., 2004, *A&A*, 428, 703

Marti, J. M., Müller E., 1994, *J. Fluid Mech.*, 258, 317

Marti, J. M., Müller E., Font J. A., Ibáñez J. M., and Marquina A., 1997, *ApJ*, 479, 151

Marti, J. M., Müller E., 2003, *Living Rev. Relativity*, 6, 7

Mészáros P., Rees M. J., 1992, *MNRAS*, 258, 41P

Mészáros P., Rees M. J., 1997, *ApJ*, 476, 232

Mészáros, P., Meszaros, P., 2006, *Rep. Prog. Phys.*, 69, 2259

Metzger, M. R., Djorgovski, S. G., Kulkarni, S. R., Steidel, C. C., Adelberger, K. L., Frail, D. A., Costa, E., Frontera, F., 1997, *Nature*, 387, 879

Mimica, P. Aloy, M. A., Müller E., *astro-ph/0611765*

Mignone, A., Plewa, T., Bodo, G., 2005, *ApJS*, 160, 199

Oren, Y., Nakar, E., Piran, T., 2004, *MNRAS*, 353, L35

Panaiteescu, A., Wen, A., Laguna, P., Mészáros, P., 1997, *ApJ*, 482, 942

Panaiteescu A., 2005, *MNRAS*, 363, 1409

Panaiteescu, A., Mészáros, P., 1999, *ApJ*, 526, 707

Panaiteescu, A., Kumar 2002, *ApJ*, 571, 779

Panaiteescu, A., Kumar 2003, *ApJ*, 592, 390

Piner, B. G., Unwin, S. C., Wehrle, A. E., Zook, A. C., Urry, C. M., & Gilmore, D. M. 2003, *ApJ*, 588, 716

Piran, T., 2000, *Physics Reports*, 333, 529

Piran, T., 2005, *Rev. Mod. Phys.*, 76, 1143

Piro et al., 1998, *A&A*, 331, L41

Pons J. A., Martí, J. M., Müller E., 2000, *J. Fluid Mech.*, 422, 125

Rhoads, J. E., 1993, *ApJ*, 591, 1097

Rhoads, J. E., 1997, *ApJ*, 478, L1

Rhoads, J. E., 1999, *ApJ*, 525, 737

Sahu, K. C., Livio, M., Petro, L., Macchett, F. D., van Paradijs, J., Kouveliotou, C., Fishman, G. J., Meegan, C. A., Groot, P. J., Galama, T., 1997, *Nature*, 387, 476

Sari R., Piran T., 1995, *ApJL*, 455, L143

Sari, R., Piran, T., & Narayan, R., 1998, *ApJL*, 497, L17

Sari R., Piran T., 1999, *ApJL*, 517, L109

Sari R., Piran T., & Halpem, J. P., 1999, *ApJ*, 519, L17

Shemi, A., Piran, T., 1990, *ApJ*, 365, L55

Soderberg A. M., Ramirez-Ruiz E., 2001, AIP conf. Proc. 662: Gamma-Ray Burst and Afterglow Astronomy 2001, pp172-175

Stanek, K. Z., Garnavich, P. M., Kaluzny, J., Pych, W., Thompson, I., 1999, *ApJ*, 522, 39L

G. Tóth and D. Odstrčil, 1996, *J. Comput. Phys.*, 128, 82.

van der Holst B., Keppens R., 2006, *J. Comput. Phys.*, submitted

Van Marle A. J., N. Langer, A. Achterberg, G. Garcia-Segura, 2006, *astro-ph/0605698*

Van Paradijs, J., et al. , 1997, *Nature*, 386, 686

Vietri, M. , 1997, *ApJ*, 478, L9

Wijers, R. A. et al., 1999, *ApJ*, 523, L33

Wijers, R., 1997, *Nature*, 393, 13

Woodward, P., Colella, P., 1984, *J. Comput. Phys.*, 54, 115

Woods E., Loeb A., 1995, *ApJ*, 453, 583

Zhang, B., et al., 2006, *ApJ*, 642, 354

Zhang W., MacFadyen A. I. , 2006, *ApJS*, 164, 255